GEOPHYSICS, VOL. 75, NO. 5 (SEPTEMBER-OCTOBER 2010); P. 75A3–75A13, 16 FIGS.
10.1190/1.3467825

Interpretation of AVO anomalies

Douglas J. Foster[1], Robert G. Keys[1], and F. David Lane[1]

ABSTRACT

We investigate the effects of changes in rock and fluid properties on amplitude-variation-with-offset (AVO) responses. In the slope-intercept domain, reflections from wet sands and shales fall on or near a trend that we call the fluid line. Reflections from the top of sands containing gas or light hydrocarbons fall on a trend approximately parallel to the fluid line; reflections from the base of gas sands fall on a parallel trend on the opposing side of the fluid line. The polarity standard of the seismic data dictates whether these reflections from the top of hydrocarbon-bearing sands are below or above the fluid line. Typically, rock properties of sands and shales differ, and therefore reflections from sand/shale interfaces are also displaced from the fluid line. The distance of these trends from the fluid line depends upon the contrast of the ratio of P-wave velocity V_P and S-wave velocity V_S. This ratio is a function of pore-fluid compressibility and implies that distance from the fluid line increases with increasing compressibility. Reflections from wet sands are closer to the fluid line than hydrocarbon-related reflections. Porosity changes affect acoustic impedance but do not significantly impact the V_P/V_S contrast. As a result, porosity changes move the AVO response along trends approximately parallel to the fluid line. These observations are useful for interpreting AVO anomalies in terms of fluids, lithology, and porosity.

INTRODUCTION

Amplitude-variation-with-offset (AVO) analysis of seismic reflections has become an important tool for hydrocarbon prospecting. However, this has not always been the case.

Early work by Muskat and Meres (1940) indicated that angle of incidence had little impact on P-wave reflections. With limited information about the elastic properties of sedimentary rocks, they assumed a constant value for Poisson's ratio throughout their study. Koefoed (1955) investigated the effect of Poisson's ratio on the angle-dependent P-wave reflection coefficient, finding that a change in Poisson's ratio at a reflecting interface can cause a significant angle-dependent variation in the P-wave reflection coefficient. The importance of Koefoed's observations became evident after the effect of pore fluids on the elastic properties of sedimentary rocks was recognized.

Measurements derived from gas- and brine-saturated sandstones by Gregory (1976) and Domenico (1977) show that Poisson's ratio, or the related ratio of P-wave velocity to S-wave velocity (V_P/V_S), is significantly affected by pore fluid. Ostrander (1984) combined these observations to show how the AVO reflection response can be used to distinguish seismic amplitudes caused by gas sands from bright reflection amplitudes caused by nonhydrocarbon-bearing rocks such as basalts. He presented numerous examples of gas sands that produce reflections with increased amplitude at the far offsets because of their V_P/V_S contrast with surrounding rocks. The gas sands studied in his work have low acoustic impedance compared to surrounding shales.

Other types of hydrocarbon-related AVO responses are identified by Rutherford and Williams (1989), who consider the effects of acoustic-impedance contrasts. They describe the seismic AVO response of gas sands that have similar or higher acoustic impedance than the encasing shales. Their work has led to a classification system for AVO responses that has been universally adopted for oil and gas exploration.

The recognition that hydrocarbons affect the acoustic impedance and Poisson's ratio of reservoir sandstones led to the development of seismic attributes to detect these effects. Some common AVO attributes are the reflection-coefficient intercept or normal-incidence reflection coefficient A; the reflection-coefficient gradient or reflection-coefficient slope at normal incidence B; P-wave normal-incidence reflectivity R_P, which is equivalent to intercept A; and S-wave normal-incidence reflectivity R_S. Most of these attributes originate with Aki and Richards' (1980) approximation for the angle-dependent P-wave reflection coefficient. From simplifications of Aki and Richards' approximation, Fatti et al. (1994) derive an expression for the P-wave reflection coefficient in terms of R_P and R_S. Similarly, Verm and Hilterman (1995) derive an expression for the angle-dependent P-wave reflection coefficient in terms of normal-incidence

Manuscript received by the Editor 30 November 2009; revised manuscript received 5 February 2010; published online 14 September 2010.

[1] ConocoPhillips, Houston, Texas, U.S.A. E-mail: douglas.j.foster@conocophillips.com; robert.g.keys@conocophillips.com; f.d.lane@conocophillips.com.

reflectivity (*NI* or A) and Poisson reflectivity *PR*. Smith and Gidlow (1987) combine Aki and Richards' approximation with the mudrock line (Castagna et al., 1985) to define the fluid factor ΔF.

Castagna and Smith (1994) compare several of these seismic attributes using velocity and density measurements from a worldwide collection of brine sands, gas sands, and shales. They find that the AVO product $A*B$ detects low-impedance gas sands of the sort described by Ostrander (1984) but is ambiguous when it comes to distinguishing high-impedance gas sands or gas sands with little impedance contrast from brine sands or shales. On the other hand, the reflectivity difference $R_P - R_S$ and $(A+B)/2$ distinguish gas sands from brine sands, regardless of acoustic impedance.

Using the same data set, Smith and Sutherland (1996) show that ΔF is also able to distinguish gas sands from brine sands, independent of the acoustic impedance of the gas sand. Sands can have higher or lower acoustic impedance than surrounding shales, but gas sands generally have a much lower Poisson's ratio than shales or brine sands. The seismic attributes $(R_P - R_S)$, $(A+B)/2$, ΔF, and *PR* tend to highlight contrasts in Poisson's ratio and thus are robust gas-sand indicators. The attributes A, R_P, and *NI* are equivalent indicators of acoustic-impedance contrasts. These can be paired with gradient B, R_S, or *PR* to interpret lithology and pore fluid (Foster et al., 1993; Verm and Hilterman, 1995; Castagna et al., 1998).

Reflectivity attributes describe contrasts in elastic properties at a welded interface and can be converted to impedance attributes by inversion. For example, R_P and R_S can be inverted to obtain P-wave and S-wave impedance. Goodway et al. (1997) use these impedances to compute the elastic properties $\lambda\rho$ and $\mu\rho$, where λ and μ are the Lamé parameters and ρ is density. Connolly (1999) introduces the concept of elastic impedance by generalizing the inversion of a normal-incidence stack to the case of variable angle of incidence. He shows how, for appropriate assumptions, elastic impedance can be derived from Aki and Richards' (1980) approximation for the angle-dependent reflection coefficient. More recently, Masters et al. (2009) generalize the AVO attributes to incorporate a probabilistic classification scheme. This provides a Bayesian-derived estimate of the uncertainty of the attributes.

In this paper, we focus on the AVO attributes intercept A and slope B. Most of the attributes previously discussed can be related to A and B through the Aki and Richards (1980) approximation. Using A and B is advantageous because they relate directly to the angle-dependent seismic data. It is easy to predict the effect that a change in A or B will have on a common-depth-point (CDP) gather or angle stacks. Thus, understanding the impact of changes in reservoir properties on A and B provides insight when interpreting the seismic-amplitude response.

We begin by analyzing the effect of changes in elastic properties on intercept and slope. We show that the key elastic properties which control the angle-dependent reflection coefficient are acoustic-impedance contrast and contrast in Poisson's ratio, or, equivalently, V_P/V_S. From this analysis, we can explain the AVO behavior observed by Rutherford and Williams.

Our analysis is based on Aki and Richards' (1980) approximation. Because this is a linear approximation that assumes small perturbations in elastic properties, we investigate the consequences of the small contrast assumption. We include a discussion on the effect of large or nonlinear changes in elastic properties.

From our analysis on the effects of elastic properties on the AVO response, we determine the effects of changes in reservoir properties, such as pore fluids, porosity, and clay content, on the seismic AVO response. Two examples illustrate these principles. The first example demonstrates the use of AVO methods to detect hydrocarbon-bearing sands, and the second illustrates the use of AVO as a lithology identifier to distinguish reservoir sands from shale.

We begin with our analysis of how changes in elastic properties affect the seismic AVO response.

Effects of elastic-property changes on AVO

For relatively small angles of incidence, usually less than 30°, Shuey (1985) shows that the compressional-wave reflection coefficient R can be approximated by an equation of the form

$$R(\theta) = A + B\sin^2(\theta). \tag{1}$$

In equation 1, θ is the angle of incidence, A is the intercept and B is the slope of the reflection coefficient evaluated at zero offset. A derivation of these results is given in Appendix A.

For small perturbations in velocity and density at a reflecting interface, the intercept and slope can be approximated by

$$A = \frac{\Delta V_P}{2V_P} + \frac{\Delta\rho}{2\rho} \tag{2}$$

and

$$B = \frac{\Delta V_P}{2V_P} - 4\frac{V_S^2}{V_P^2}\left\{\frac{\Delta\rho}{2\rho} + \frac{\Delta V_S}{V_S}\right\}. \tag{3}$$

In equations 2 and 3, V_P, V_S, and ρ are the averages of the compressional-wave velocity, shear-wave velocity, and density above and below the reflecting interface, respectively; ΔV_P, ΔV_S, and $\Delta\rho$ are the differences in compressional-wave velocity, shear-wave velocity, and density between these layers, respectively.

Let $\gamma = V_S/V_P$ and $\Delta\gamma$ represent the difference in this ratio between the layer below and the layer above the reflector. Neglecting second-order terms,

$$\frac{\Delta\gamma}{\gamma} = \frac{\Delta V_S}{V_S} - \frac{\Delta V_P}{V_P}. \tag{4}$$

Substituting equation 4 into 3 and combining with equation 2 shows that

$$B = (1 - 8\gamma^2)A - 4\gamma\Delta\gamma + (4\gamma^2 - 1)\frac{\Delta\rho}{2\rho}.$$

The assumption that $V_P/V_S = 2.0$ is often a good approximation for normally pressured shale. If the ratio γ is close to 0.5 ($V_P/V_S = 2.0$), the last term can be neglected as a second-order perturbation, yielding

$$B = (1 - 8\gamma^2)A - 4\gamma\Delta\gamma. \tag{5}$$

In a crossplot of A versus B, equation 5 describes a family of lines that is approximately parallel to the line:

$$B = (1 - 8\gamma^2)A. \tag{6}$$

We call this the fluid line.

Equation 5 shows that in the crossplot domain, reflections are characterized by their contrasts in acoustic impedance and V_P/V_S relative to the fluid-line trend. An intercept and gradient crossplot based on equation 5 is depicted in Figure 1. AVO responses at the top of sand are shown for the four classes of gas sands identified by Rutherford and Williams (1989) and Castagna and Swan (1997). The slope of the fluid line depends on the background V_P/V_S (or $V_P/V_S = 1/\gamma$). The fluid-line slope is -1 if $V_P/V_S = 2$ and rotates counterclockwise as V_P/V_S increases. These observations about the fluid line hold whether the background V_P/V_S is constant or slowly varying (Castagna et al., 1998).

The fluid line is a useful concept because reflections from shales and some wet sands that have little contrast in V_P/V_S tend to fall near the fluid-line trend; reflections from hydrocarbon-bearing sands usually do not. Equation 5 suggests that an abrupt decrease in V_P/V_S of the medium below the reflecting interface will cause the slope-intercept pair to fall below the fluid-line trend. The latter trend is displaced from the fluid line by an amount proportional to $-4\gamma\Delta\gamma$. Because gas or light hydrocarbons often cause an abrupt decrease in V_P/V_S of porous sand, reflections from the tops of hydrocarbon-bearing sands fall on a trend below the fluid line. Similarly, a sharp increase in V_P/V_S at the base of a hydrocarbon-bearing sand places the slope-intercept pair on a trend above the fluid line. Thus, displacement from the fluid line can distinguish hydrocarbon-bearing sands from wet sands and shales. If there is a significant V_P/V_S contrast between sands and shales, this analysis can be used to predict lithology in clastic sediments.

Rutherford and Williams (1989) define three classes of AVO responses based on acoustic impedance contrasts. Castagna and Swan (1997) add a fourth class of gas sands. When analyzing bandlimited seismic data, however, this classification may not be straightforward and is typically subjective.

Figure 1 depicts the AVO response of reflections from the tops of the four classes of gas sands. The four classes are aligned on a trend in the figure. This is a consequence of equation 5. Batzle et al. (1995) show that the V_P/V_S contrast depends on the type of pore fluid. Therefore, the AVO response of the four classes of gas sands must fall on the trend that corresponds to the V_P/V_S contrast for gas sands. As equation 5 shows, their position on the gas-sand trend depends on their acoustic-impedance contrast with the surrounding rocks.

A class I gas sand (a gas sand that produces a reflection characterized as class I) has higher acoustic impedance than the encasing shale. From equation 5, a reflection from the top of a class I gas sand must lie below the fluid-line trend, to the right of the slope axis. Therefore, the reflection from the top of a class I gas sand is positive at normal incidence, but its amplitude decreases with increasing offset faster than reflections that fall on the fluid-line trend. The reflection coefficient may become negative, or reverse polarity, with increasing offset.

If the acoustic impedance of the gas sand is reduced to that of the surrounding shale, it becomes a class II gas sand. The slope-intercept point for a class II gas sand lies at or near the intersection of the gas-sand trend with the slope axis. The reflection from the top of a class II gas sand is negligible at zero offset but has a negative slope, so its amplitude becomes large in magnitude with respect to the zero-offset amplitude and negative with increasing angle.

Reducing acoustic impedance further leads to a class III gas sand that has lower impedance than the overlying shale. Figure 1 shows that the reflection from the top of a class III gas sand has negative intercept and slope; consequently, it is negative at normal incidence and becomes more negative with increasing angle.

Continuing to decrease the acoustic impedance moves the reflection intercept-slope point up and to the left on the gas sand trend to produce a class IV gas-sand reflection, characterized by a negative intercept and a slope that is zero or positive. The reflection from the top of a class IV gas sand is negative, but its magnitude does not increase with angle.

Exact *A*s and *B*s

Equation 5 is based on intercept and slope approximations that assume small perturbations in elastic properties at a reflecting interface. Although these approximations are adequate for modeling the angle-dependent behavior of the compressional-wave reflection coefficient, one might question whether they are accurate enough to describe the relationship between intercept and slope. In other words, what are the consequences of neglecting the second-order perturbations that lead to equation 5?

Exact equations for intercept and slope based on the Zoeppritz equations (Achenbach, 1973, p. 186) are given by Foster et al. (1997, p. 199). For general media, it is difficult to transform these equations into a relation between slope and intercept. However, a relation between slope and intercept can be derived for special cases. In particular, if we assume the density contrast is negligible across the reflecting interface, then the exact intercept and slope satisfy the equation

$$B = (1 - 8\gamma^2)A - 4\gamma\Delta\gamma(1 - \Delta\gamma) + (1 - 2\gamma)O(A^2). \tag{7}$$

In equation 7, second-order perturbations are retained, but third-order and higher perturbations are neglected. A derivation of this equation is provided in Appendix A.

If V_P/V_S is close to two, then $(1 - 2\gamma)$ behaves like a perturbation of γ, and the last term on the right of equation 7 can be regarded as third order. Although density contrasts are neglected, the exact slope and intercept values calculated using equations A-3 and A-4 with input data from sonic and density logs match trends predicted by equation 7 very well (see Figure 2b). The log data are measured V_P and ρ, but V_S is computed from V_P. Figure 2a shows the dependence of the intercept and slope trend (fluid line) on the background V_P/V_S. When there is a V_P/V_S contrast, Figure 2b shows that points deviate from the background fluid-line trend consistent with equation 7. In Figure 2, the attributes are calculated at the sample rate of the well-log data.

There are two obvious differences between equations 5 and 7 that have practical significance. First, the error term in equation 7 shows that second-order perturbations in A vanish when $\gamma = 0.5$, which

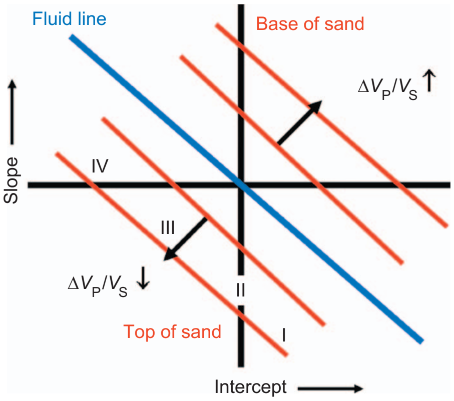

Figure 1. Intercept *A* versus slope *B* crossplot. AVO responses at top of sand are shown for the four classes of gas sands. The polarity convention for this plot denotes a decrease in acoustic impedance by a negative amplitude (trough).

means the linear relationship between slope and intercept is most accurate when V_P/V_S is near 2.0. When $V_P/V_S > 2.0$, there is more scatter from the trend that is unrelated to changes in V_P/V_S. Additionally, the density term that was omitted in equation 5 becomes more significant. This is evident in Figure 2a, where the slope and intercept are strongly correlated when $V_P/V_S = 2.0$ but are less correlated when V_P/V_S is different from 2.0. Also, for larger magnitudes of A, the background trend is not linear.

These results suggest that AVO methods which use distance from a background trend to detect hydrocarbons are often more effective in sediments where the background V_P/V_S is close to 2.0. In shallow, unconsolidated sediments where $V_P/V_S > 2.0$, the background trend will be less correlated. This can also be true in overpressured sediments where the background V_P/V_S can exceed 2.0 at great depths. Intercept or normal-incidence reflectivity can be a better hydrocarbon indicator in shallow, unconsolidated sands than an AVO anomaly. Note that class III or IV gas sands may produce a large intercept or normal-incidence reflection coefficient. Polarity is important in this case.

The second difference between equations 5 and 7 is the perturbation term containing $\Delta\gamma$. Equation 7 implies that trends resulting from changes in γ are not symmetric with respect to the fluid line. If all other factors are equal, base-of-sand reflections lie farther from the fluid-line trend than top-of-sand reflections. Although symmetric with respect to normal-incidence reflectivity, equation 7 predicts that the AVO slope B response from the base of sand should be more prominent than the slope from the top of sand. This asymmetry is a second-order effect, but it is evident in Figure 2b. The asymmetry becomes greater as the V_P/V_S contrast increases. Actually, it is fortunate that base-of-sand reflections have this enhanced AVO response because they can be used to identify downdip limits that provide further support for the presence of hydrocarbons. This enhanced response can be seen in the B attribute and any other attributes that are a function of the slope (e.g., fluid line, Poisson reflectivity, fluid factor, $A + B$). As a second-order effect, this asymmetry may not be visible on a conventional seismic section for thin sands. In practice, the best opportunity to observe the effect is with relatively thick reservoirs bounded by a uniform shale that produces no interference between the top and base reflections.

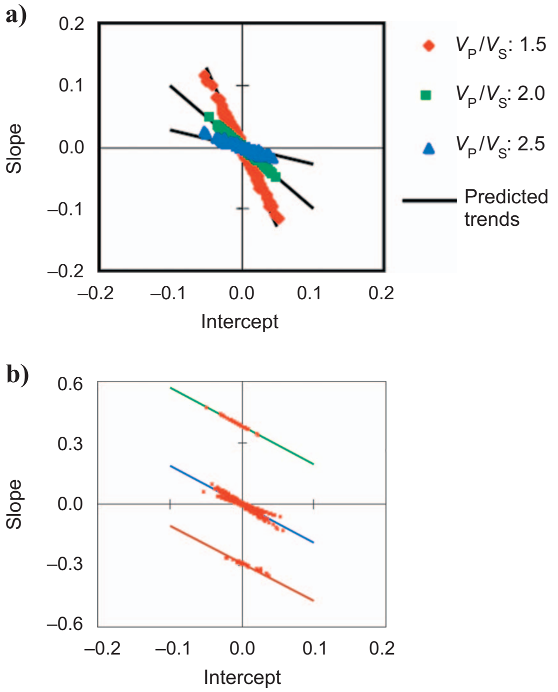

Figure 2. Comparison of predicted trends from equation 7 with slope and intercept values calculated using sonic and density logs from well A (Keys and Foster, 1998). (a) Shear-wave velocities derived using $V_P/V_S = 1.5$ (red), 2.0 (green), and 2.5 (blue). (b) Shear-wave velocities derived using $V_P/V_S = 1.9$ for background rocks and 1.5 for sands.

Effects of rock- and fluid-property changes on AVO

Up to this point, we have considered the effects of changes in elastic properties such as acoustic impedance and V_P/V_S on the seismic AVO response. The more important issue is the effect of changes in rock and fluid properties on the response. One property that has a significant effect is pore-fluid compressibility.

Replacing brine with a highly compressible pore fluid such as gas or light oil reduces the compressional-wave velocity of the rock. Although the shear modulus is unaffected by the type of pore fluid, the shear-wave velocity increases slightly because of the lower density of hydrocarbons. Consequently, increasing pore-fluid compressibility significantly reduces the V_P/V_S of the rock. Equations 5 and 7 show that an abrupt change in V_P/V_S displaces the AVO response from the fluid-line trend by an amount dependent on the V_P/V_S contrast. The magnitude of the displacement from the fluid line increases as pore-fluid compressibility increases.

The effect of pore-fluid compressibility on AVO responses is depicted in Figure 3. This effect is similar to the results obtained by Batzle et al. (1995) for various pore fluids, including 20° API oil, 50°API live oil, and gas. Gas, with the highest compressibility, produces the greatest departure from the fluid-line trend, followed by 50°API live oil. Heavier oils with low gas content approach the response of brine-saturated sands.

Porosity is another rock property that has a significant effect on seismic response. An increase in porosity decreases compressional-wave velocity and density. Unlike fluid compressibility, which has little effect on shear-wave velocity, an increase in porosity also decreases shear-wave velocity. The decrease in shear-wave velocity offsets the decrease in compressional-wave velocity so that V_P/V_S is not significantly changed. Brie et al. (1995), for example, report a V_P/V_S of 1.58 for clean gas sands, irrespective of porosity.

The effect of porosity changes on the AVO response are illustrated in Figure 3. Because increasing the porosity of a gas sand reduces its acoustic impedance, the intercept A of a reflection from the top of the sand becomes more negative and moves to the left in Figure 3. However, because porosity changes do not affect the V_P/V_S contrast, the slope-intercept value of the reflection remains on a trend defined by the initial V_P/V_S contrast.

To illustrate how porosity affects the AVO response of a seismic reflection, suppose we observe a reflection from the top of a class III gas sand designated by point 1 in Figure 3. At normal incidence, the reflection from this sand is negative and becomes more negative with increasing offset. If we increase the porosity of this gas sand, its AVO response will move in the direction of the arrow denoting increasing porosity in Figure 3 to point 2. At this new location, the reflection is larger in magnitude (more negative) but has less variation with offset than the reflection at point 1. Alternatively, if we reduce the porosity of the gas sand, we will move toward point 3 on the crossplot. The resulting reflection will have a small amplitude at normal incidence but will increase in magnitude (become more negative) with increasing angle of incidence. The amplitude increase with angle is greater at point 3 than at point 1 or 2. The reflection at point 4 results from replacing gas with brine. Reducing the porosity of the brine-saturated sand will move the reflection from 4 to 5 on the crossplot. The reflection at point 5 will be large and positive at zero offset, and its amplitude will decrease in magnitude with increasing angle.

In addition to porosity and pore fluid, shale content affects the seismic AVO response. However, the impact of shale content on AVO characteristics is complex. Figure 3 depicts the AVO effects of increasing shale content based on the sand-clay mixture model described by Marion et al. (1992). Consider the wet-sand point 4 in Figure 3. Increasing the shale content by adding clay to the pore space increases acoustic impedance by reducing porosity. Also, increasing shale content increases V_P/V_S because the slope and intercept response of pure shale must lie on the fluid line. Therefore, increasing shale content moves the AVO response in the direction of the solid brown arrow, which is in the direction of reduced porosity but closer to the fluid line.

Clay can be added to the pore space until critical concentration is reached. At this point, the pore space is filled with clay, and additional clay cannot be added without displacing grains of sand. Increasing shale content beyond the critical concentration reduces acoustic impedance and moves the AVO response in the direction of the dashed brown arrow. The start and end points of the shale-content arrows depend on the pure-sand and pure-shale porosities. As Figure 3 indicates, acoustic impedance can be an ambiguous discriminator between sands and shales, but sands generally have greater V_P/V_S contrast with the fluid line than shales.

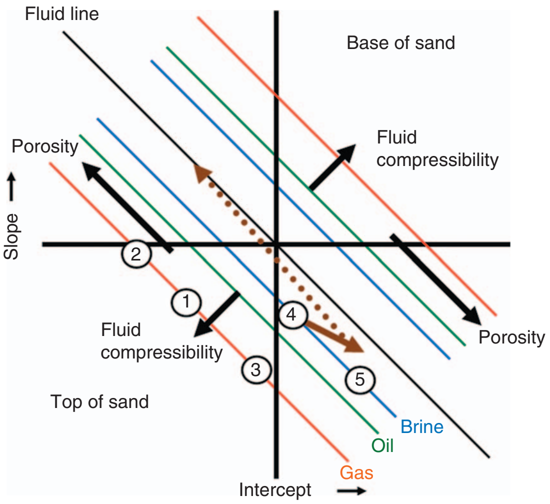

Figure 3. Effects of changes in reservoir properties on AVO response. An increase in pore-fluid compressibility displaces reflection response farther from the fluid-line trend (not necessarily in a direction perpendicular to the trend, however). An increase in porosity moves the reflection response parallel to the fluid-line trend, in the direction of the solid arrows. The numbered points on the crossplot illustrate the effect of varying porosity and pore fluid on the AVO response from top of sand: 1 — AVO response from top of a class III gas sand; 2 — AVO response of a higher-porosity gas sand; 3 — AVO response of a lower-porosity gas sand; 4 — wet-sand response obtained by replacing gas with brine; 5 — AVO response of a lower-porosity wet sand. The solid brown arrow depicts the effect of increasing shale content in a shaly sand by adding clay to the pore space until critical concentration is reached, at which point no more clay can be added to the pore space without displacing grains of sand. The dashed brown arrow shows the effect of increasing shale content in excess of the critical concentration.

The effects of pore-fluid changes in the A and B crossplot domain can be illustrated using the well-log data displayed in Figure 4. Figure 5 shows the crossplot for gas and brine against the shale background. The brine points are calculated by Gassmann fluid substitution (Mavko et al., 1998). In this plot, shale-on-shale reflections define the fluid line. Gas-sand reflections are the farthest from the fluid line, and brine sands are between the gas-sand and shale points.

Using the well-log data in Figure 4, the effects of porosity changes in the A and B crossplot domain are shown in Figure 6. The porosity trend is clearly seen in this plot. The highest-porosity sand has a class IV AVO response, and the lowest-porosity sandstones are class I to class II. This porosity trend is commonly seen in normally compacting sediments; AVO anomalies will follow this porosity/depth trend. Overpressured sediments can disrupt the trend. In normal-pressured sediments, it is unusual to see class III anomalies at significant depths below class II anomalies.

Example 1: Application of AVO analysis to hydrocarbon detection

Our first example illustrates the use of AVO analysis to differentiate light hydrocarbon (oil and gas) sands from brine sands in a structural trap with four-way dip closure. The study area is outlined in Figure 7, which shows a time structure map of the top of the reservoir interval. The structure consists of an eastern, central, and western substructure. The reservoir sands are stacked and consist of relatively thin fluvial, marine, and deltaic sands with interbedded shales. A stratigraphic column is shown in Figure 8. Two wells from the study area that encountered gas, oil, and brine sands are used for AVO analysis. Well 1 was drilled in the central structure, and well 2 is located in the western structure. Figure 9 shows a far-angle stack section through well 1 in the central structure.

The well data indicate the reservoir section is normally pressured. Porosities range from the mid- to high twenties in the top of the reservoir interval and decrease to the low twenties to high teens in the

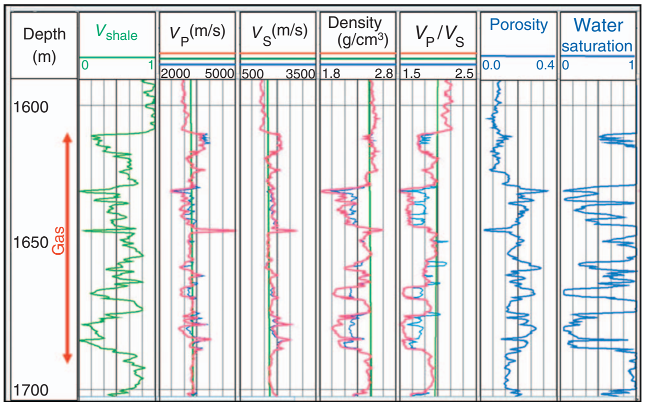

Figure 4. Log data from well 1. Track 1 — shale volume curve (green). Red curves, tracks 2–5: measured P-wave velocity, S-wave velocity, bulk density, and V_P/V_S. Green curves, tracks 2–5: shale trend curves for P-wave velocity, S-wave velocity, density, and V_P/V_S. Blue curves, tracks 2–5: P-wave velocity, S-wave velocity, density, and V_P/V_S obtained from the measured (red) curves by replacing in situ hydrocarbons with brine.

lower interval as a normal consequence of compaction and variation in rock quality, resulting from changes in depositional environment. The aim of this study is to evaluate the potential for differentiating hydrocarbons from water using AVO information and to determine the extent of hydrocarbons. There is no attempt to distinguish gas from oil because the oil is light with a high gas/oil ratio.

The first step in our analysis is to determine the expected AVO response for brine- and hydrocarbon-filled sands. We use the available well-log data to accomplish this objective. Intercept and slope crossplots derived from the two wells are shown in Figure 10. Figure 10a and b plots are from well 1; Figure 10c and d plots are from well 2 for the same formation. Figure 10a and c shows intercept and slope crossplots for reflections from top of sand and top of shale relative to the average background shale for sands and shales in the upper hy-

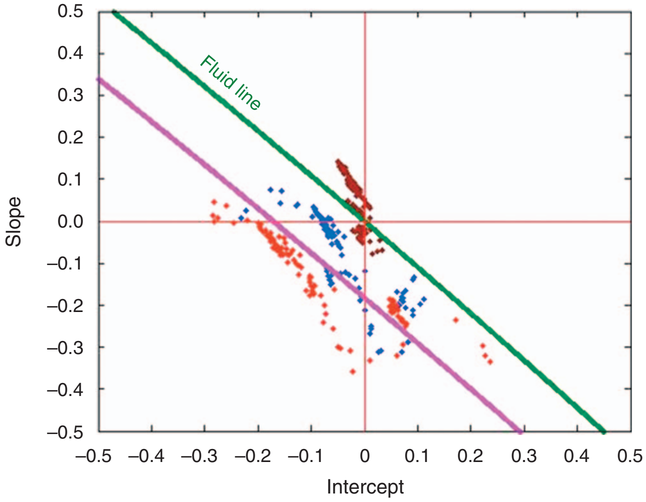

Figure 5. Slope-intercept crossplot from well 1. Red points are slope-intercept values of reflections from the background shale/sand interface for sands from well 1 between 1600 and 1692 m. Blue points correspond to reflections from the background shale/sand interface for fluid-substituted brine sands between 1600 and 1692 m. Brown points denote reflections from background shale/shale interface for shales between 1600 and 1692 m. The solid green line is the fluid line from equation 6 for the background shale V_P/V_S. The magenta line is the trend curve corresponding to a decrease in V_P/V_S from 2.0 to 1.67. Figure 4 shows that most gas sands have $V_P/V_S < 1.67$ and, as predicted by equation 5, lie below the magenta trend line.

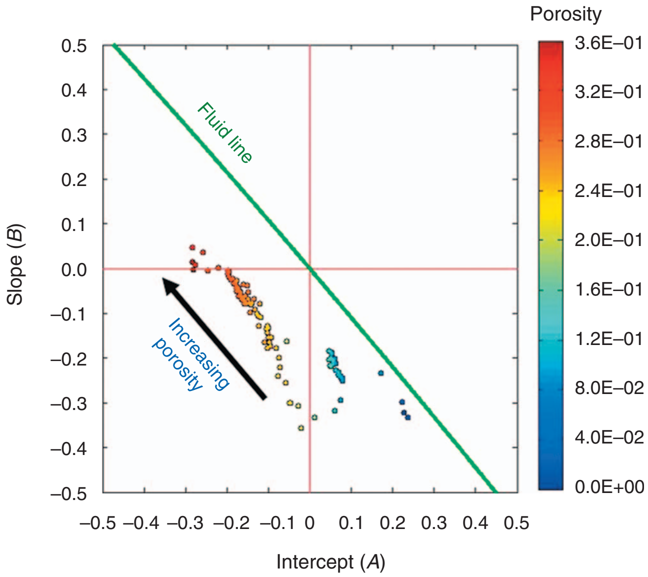

Figure 6. Slope-intercept crossplot from well 1. The points are color coded based on their porosity, red being the most porous and blue the least. These points come from reflections from the background shale/sand interface for sands in well 1 between 1600 and 1692 m. The solid green line is the fluid line from equation 6 for a background shale V_P/V_S of 1.9.

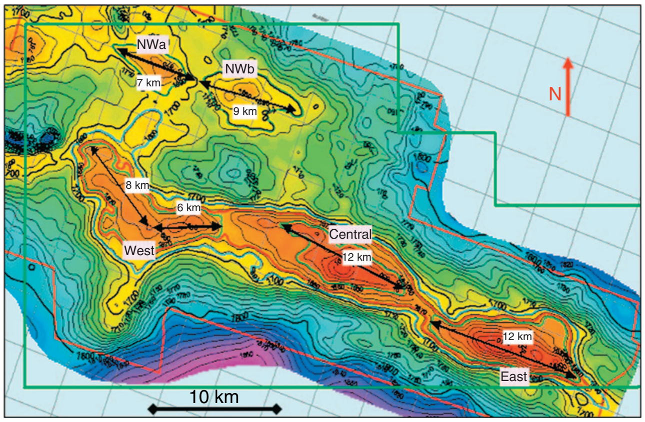

Figure 7. Time structure map from the top of the productive zone. The main structure consists of three individual structures (east, central, and west). Warmer colors (orange, yellow) represent structural highs; cooler colors (purple, blue) are structural lows.

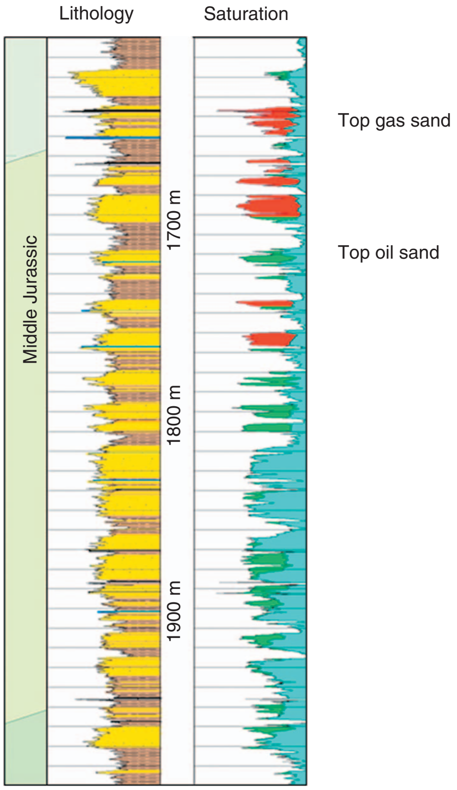

Figure 8. Stratigraphic column for well 1. The right track shows the gas- (red), oil- (green), and brine (blue) sands. The left track shows sands (yellow), shales (brown), and thin coals (black).

drocarbon-filled reservoir interval. Also shown are the intercept and slope values for reflections from top of brine sands relative to background shale. Brine-sand properties are obtained by substituting the in situ pore fluid with brine. Intercept and slope values are calculated from equations 2 and 3, using background shale properties for the overlying shale layer and the well-log data for the underlying sand or shale layer.

Figure 10b and d shows slope and intercept values derived from synthetic seismic gathers modeled from the well-log data. Intercept and slope are determined by a least-squares fit to the angle-dependent reflection coefficient. The red points are slope and intercept values from the hydrocarbon sand interval, and the blue points are from background or nonhydrocarbon-bearing reflections. Because the lower crossplots are derived from synthetic seismic data, they are affected by the seismic bandwidth. Thus, Figure 10a and c indicates the expected AVO response for individual sand units, and Figure 10b and d shows the impact of thickness and tuning.

The crossplots and seismic data for this example use the polarity convention that denotes a decrease in acoustic impedance by a positive reflection amplitude, or peak, on a seismic display. Subsequently, top-of-sand reflections lie above the fluid line and base-of-sand reflections lie below the fluid line.

Figure 10 illustrates a distinct difference in the AVO response of brine- and hydrocarbon-filled sands observed at the top of the reservoir interval. At the top of the reservoir, hydrocarbon sands have a class III response, approaching class IV. A reflection from the top of a gas sand should be a peak at zero offset and become larger with increasing angle. Figure 10 also shows that brine sands have low impedance with less separation in AVO response from background shales. This suggests that on a correctly processed seismic section, amplitudes should be observed to dim downdip from a hydrocarbon/water contact.

Similar analysis applied to deeper intervals in wells 1 and 2 shows that the expected AVO response for hydrocarbon sands ranges from class III at the top of the reservoir section to class II in the deeper section as porosity decreases. Although the brine sands are low impedance at the top of the reservoir, in general, the acoustic impedance and V_P/V_S contrast between brine sands and background shales are small, and differences in pore fluids should be evident in the seismic data. With these expectations from the analysis of the well data, we proceed to analyze the seismic data.

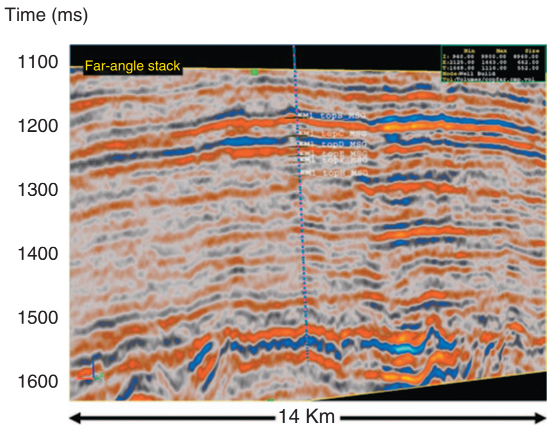

Figure 9. Far-angle stacked cross section through the well shown in Figure 4. Orange to yellow colors indicate a decrease in acoustic impedance; blue denotes an increase in acoustic impedance.

From 3D prestack-time-migrated gathers, we estimate intercept and gradient volumes. Figure 11 shows a crossplot derived from the 3D seismic data. The blue points are background data from a region downdip from the crest of the structure in a section containing wet sands and shales. The seismic response from this location is used to define the fluid line. The red points come from an updip region on the crest of the structure and in the upper portion of the reservoir interval. This part of the reservoir contains oil and gas. The AVO response in this upper portion of the reservoir is predominantly class III, as ex-

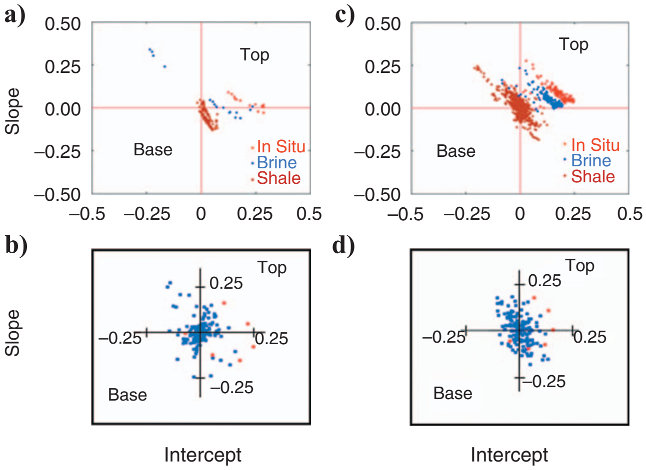

Figure 10. Slope-intercept crossplots from top gas sand in wells 1 (a, b) and 2 (c, d). (a) Slope-intercept crossplot using log data from a well in the central structure. The data are from an interval at the top of the reservoir. (b) Intercept and slope values derived from synthetic seismic data from the same interval. (c, d) Slope-intercept crossplots are similar displays from a well in the western structure.

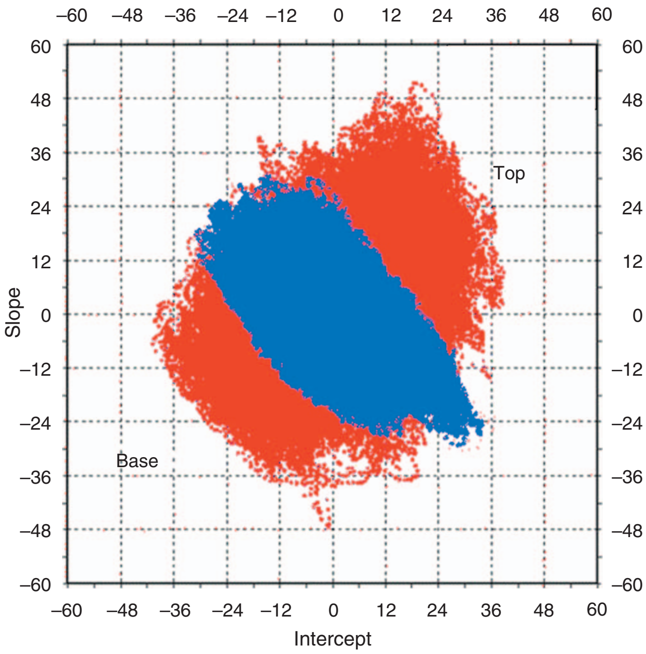

Figure 11. Slope-intercept crossplot from the 3D seismic data. The blue points (background) are derived from an area downdip from the crest of the structure containing wet sands and shales. The red points (pay) come from an area around the crest of the structure in the upper portion of the reservoir interval where hydrocarbons are expected.

pected. Using the concepts outlined earlier, we interpret the anomalies in terms of changes in pore fluids and relative-porosity variations.

Figure 12 depicts a color scheme used to classify seismic anomalies based on Rutherford and Williams' (1989) classification. Using this color scheme, a seismic cross section through well 1 highlighting AVO anomalies is shown in Figure 13a. The AVO color-class section is overlain on the near-angle (0°–15°) stack, displayed as wiggle traces. A zero-offset synthetic seismic trace is posted at the well 1 location. The AVO color section has dark-green over light-green amplitude at the crest of the structure between 1200 and 1250 ms, indicating a class III top over class III base — consistent with high-porosity gas sands. A notable characteristic of the section is that the seismic class III anomaly's downdip termination closely matches the time-converted hydrocarbon/water contact (HWC) from a multidynamic test (MDT). Throughout the section, the strength of the anomalies decreases with depth, and class II anomalies are seen at deeper depths, consistent with reduced-porosity sands.

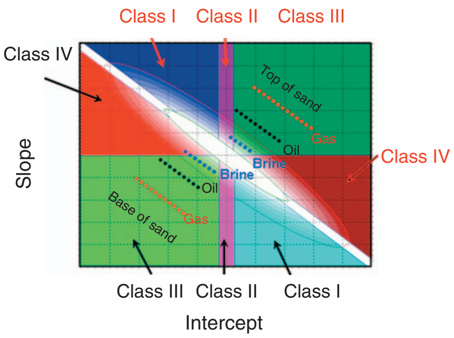

Figure 12. AVO classification scheme for identifying the magnitude and class of a seismic reflection. The polarity convention in this display denotes a decrease in acoustic impedance by a peak.

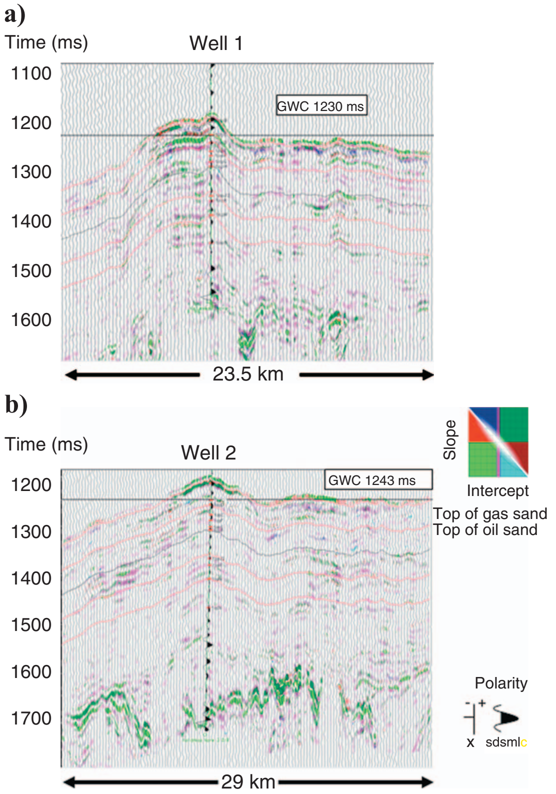

Figure 13. AVO classification scheme for a seismic line going through (a) well 1 in the central structure and (b) well 2 in the west structure. A zero-offset synthetic is displayed at the well locations. The horizontal line at 1230 ms is the hydrocarbon/water contact of the top hydrocarbon sand, determined from the multidynamic test. Background wiggle traces are the near-angle stack. GWC = gas/water contact.

An AVO color-class section through well 2 is shown in Figure 13b, overlain with the near-angle stack wiggle-trace cross section and a zero-offset synthetic trace posted at the well location. Like the cross section through well 1, there is a class III top and base (dark green/light green) AVO anomaly at the crest of the western structure. The AVO anomaly terminates downdip at the HWC (1243 ms) established from the MDT.

Map-view amplitude extractions are useful for checking conformance to structure. Figure 14 shows a horizon amplitude extraction from the top of a hydrocarbon-bearing sand using the AVO classification scheme described previously, compared with an amplitude extraction from the far-angle stack. The far-angle (20°–35°) stack, like the fluid-line attribute, is sensitive to V_P/V_S ($\Delta\gamma$) contrasts. Also shown is a constant time contour corresponding to the HWC estimated from the two wells. This anomaly shows relatively good conformance to structure. The amplitude extraction from the AVO class volume and the far-angle stack shows the anomaly extends to the eastern structure within the expected contour interval. A well in the eastern structure confirms the presence of hydrocarbons in this interval.

This analysis suggests that the seismic AVO response can distinguish hydrocarbon-bearing sands from brine sands and shales in the study area. Consequently, the seismic AVO data were used to determine the extent of hydrocarbons and to aid in the delineation of the field.

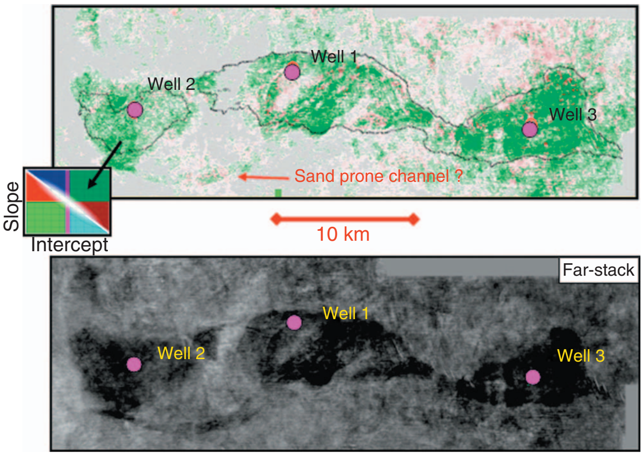

Figure 14. Amplitude extractions from the AVO classification scheme and the far-angle stack. The black line on the AVO classification plot (upper display) is a time contour at the assumed hydrocarbon/water contact. This extraction comes from the top of the reservoir. The lower plot is an amplitude extraction from a far angle stack.

Example 2: Application of AVO analysis to lithology discrimination

A second example demonstrates the use of AVO analysis for lithology prediction. In hard-rock or low-porosity reservoirs, the fluid effect on an AVO response can be negligible, but finding reservoir-quality sand is important. In this case, fluid contacts and conformance of seismic amplitude to depth structure may be difficult to discern; however, calibrated anomalies consistent with a working geologic model may be used to help map sand distribution. The reservoir in this example is a stratigraphic trap containing light hydrocarbons. Stratigraphically, we expect to see thick sands in a main channel feeding a turbidite fan. Furthermore, porosities are expected to decrease in a direction distal to the sediment source.

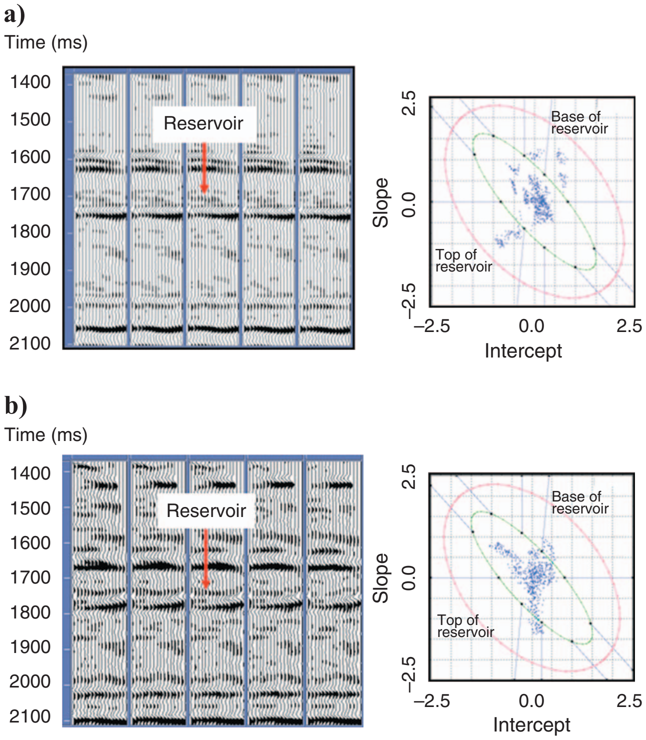

Figure 15. Gathers around (a) well A and (b) well B locations and the crossplots derived from the data. These data in the crossplot are from the reservoir interval. At the well A location (a), there is a class III anomaly, indicating relatively high porosity. At the well B location (b), there is a class II anomaly, indicating relatively low porosity.

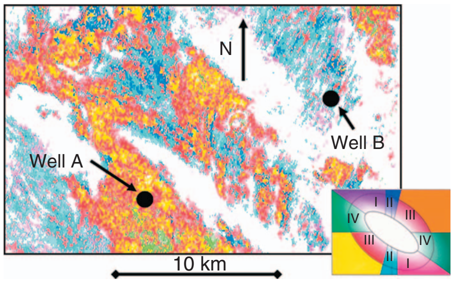

Figure 16. Amplitude extraction along the top reservoir reflection from the AVO classification volume. Well A shows a relatively strong class III anomaly, and well B shows a class II anomaly. The porosity in well A is higher than the porosity in well B.

As a general rule, class II anomalies are associated with sands of lower porosity than sands that produce class III anomalies. An example of this is shown in Figures 15 and 16. This example assumes the polarity convention that a peak denotes an increase in acoustic impedance. Figure 15a shows the seismic gathers and a crossplot of the intercept and slope derived from data around well A. The crossplot and gathers indicate a class III response for the reservoir. Evidence of this is seen at the near offset, where there is a trough-and-peak pair. The porosity in this well is high enough that the reservoir is considered to be commercial. Figure 15b shows data from an area around well B. At this location, there is very little energy on the near offsets and significant energy at the far offsets. The AVO response is class II. Here, the porosity is lower than that encountered in well A. The reservoir porosity at well B is below the commercial threshold.

Figure 16 shows the AVO class response in map view. The threshold used to create this map highlights the cleanest sands (farthest from the fluid-line trend). This extraction is taken from the reflection at the top of the reservoir interval. In Figure 16, red and yellow colors represent class III reflections, and blue colors denote class II events. Well A penetrated the reservoir, which has a strong class III anomaly, and found relatively clean, hydrocarbon-bearing sand with good porosity. Well B, however, penetrated a class II anomaly and found hydrocarbon sand with poorer porosity. This plot identifies the preferred porosity zones based on the theoretical model described above. The results discussed here were used in the exploration and appraisal phases of this area.

CONCLUSIONS

Exact expressions for intercept and slope show that the fluid-line trend has the least scatter when $V_P/V_S = 2$. In this case, density contrasts do not contribute to the scatter of points about the trend. Analysis of second-order effects shows the reflection-coefficient slope is enhanced by an increase in V_P/V_S and diminished by a decrease in V_P/V_S. Consequently, all other factors being equal, the gradient of the reflection coefficient from the base of sand is more prominent than the top-of-sand reflection-coefficient gradient. This knowledge may aid in determining the downdip extent of the anomaly. Slope and intercept crossplots are useful for interpreting AVO anomalies and explaining the effects of changes in rock and pore-fluid properties. As pore-fluid compressibility increases, the slope and intercept points move away from the fluid line. This can aid in discriminating hydrocarbon from brine sands. Gas causes the largest deviation from the trend, and brine has the least; oil-sand points lie in the region between, based on specific oil properties.

Typically, there is a contrast in V_P/V_S between clean sand and shale. This contrast produces a deviation in the seismic AVO response of clean sands from the background trend. Porosity variations affect acoustic impedance but do not significantly affect V_P/V_S; therefore, porosity variations move points approximately parallel to the fluid line. These observations can be used to discriminate reservoir quality and to distinguish sand from shale. AVO classes can indicate relative changes in porosity. In a relative sense, the highest-porosity gas sands result in a class IV event, and the lowest-porosity gas sands are characterized by class I reflections. It is important that any AVO anomaly be interpreted within the context of an appropriate geologic model. The principles described here are useful for gaining insight into the geologic controls responsible for the character of AVO anomalies.

ACKNOWLEDGMENTS

We acknowledge Jeff Malloy, Scott Irvine, Erik Keskula, Jon Anderson, Duncan Emsley, Tim Wallace, Mike Faust, and Renee Hannon for their contributions. In addition, we are grateful to reviewers Fred Hilterman, Ron Masters, Benoit Paternoster, and the associate editor for their insight and constructive comments. We thank ConocoPhillips for permission to publish this work.

APPENDIX A

SECOND-ORDER RELATIONSHIP BETWEEN *A* AND *B*

The derivation of equations 5 and 7 and the attributes A and B (equations 2 and 3), linearized with respect to medium property contrasts, is given in Foster et al. (1997). We summarize the results below.

The coefficients of the reflected R and transmitted T plane waves at an interface between two elastic solids are determined by the conditions that normal and tangential components of stress and displacement must be continuous. In matrix form (Achenbach, 1973, p. 186), the four equations are

$$M\begin{bmatrix} R_{PP} \\ R_{PS} \\ T_{PP} \\ T_{PS} \end{bmatrix} = \begin{bmatrix} x \\ \sqrt{1-x^2} \\ 2b^2x\sqrt{1-x^2} \\ 1-2b^2x^2 \end{bmatrix}, \tag{A-1}$$

where M is the matrix

$$\begin{bmatrix} -x & -\sqrt{1-b^2x^2} & cx & -\sqrt{1-d^2x^2} \\ \sqrt{1-x^2} & -bx & \sqrt{1-c^2x^2} & dx \\ 2b^2x\sqrt{1-x^2} & b(1-2b^2x^2) & 2ad^2x\sqrt{1-c^2x^2} & -ad(1-2d^2x^2) \\ -(1-2b^2x^2) & 2b^2x\sqrt{1-b^2x^2} & ac(1-2d^2x^2) & 2ad^2x\sqrt{1-d^2x^2} \end{bmatrix} \tag{A-2}$$

and where $a=\rho_2/\rho_1$, $b=\beta_1/\alpha_1$, $c=\alpha_2/\alpha_1$, $d=\beta_2/\alpha_1$, and $x=\sin\theta$. The angle θ is the angle of incidence, measured counterclockwise from the normal to the reflecting boundary. The parameters characterizing the properties of the lower half-space α_2, β_2, and ρ_2 are the compressional velocity, shear velocity, and density, respectively. The parameters α_1, β_1, and ρ_1 are similarly defined for the upper half-space. The compressional and converted shear reflection coefficients are R_{PP} and R_{PS}, and the compressional and converted shear transmission coefficients are T_{PP} and T_{PS}.

Let D denote the determinant of M, and let N be the determinant of the matrix obtained by replacing the first column of M with the vector on the right-hand side of equation A-1. The compressional-wave reflection coefficient is given by $R_{PP}=N/D$.

The derivation of equation 1 assumes relatively small angles of incidence. With this assumption, R_{PP} is approximated with a Taylor-series expansion with respect to $\sin^2\theta$, (x^2) evaluated at $\theta=0$. From Foster et al. (1997), the expressions for A and B for arbitrarily large contrasts are

$$A=\frac{ac-1}{ac+1} \tag{A-3}$$

and

$$B=\frac{8k[k-ac(b+d)]+ac[(c^2-1)(b+ad)-2(1-a)^2bcd]}{(ac+1)^2(b+ad)}. \tag{A-4}$$

In equation A-4, $k=ad^2-b^2$. Equation A-3 is the exact zero-offset reflection coefficient A, and equation A-4 is the exact slope B, or derivative of the reflection coefficient with respect to $\sin^2(\theta)$ at zero offset.

The small contrast approximations, given in equations 2 and 3, are derived by defining $\rho=(\rho_2+\rho_1)/2$, $\Delta\rho=(\rho_2-\rho_1)$, $\alpha=(\alpha_2+\alpha_1)/2$, $\Delta\alpha=(\alpha_2-\alpha_1)$, $\beta=(\beta_2+\beta_1)/2$, and $\Delta\beta=(\beta_2-\beta_1)$; then substituting these expressions into equations A-3 and A-4 and retaining only first-order terms.

Assuming the density contrast is negligible,

$$c=\frac{1+A}{1-A}, \tag{A-5}$$

where $a=1$, $b=\gamma_1$, $d=c\gamma_2$, $\gamma_1=\beta_1/\alpha_1$, and $\gamma_2=\beta_2/\alpha_2$. Substituting these into equation A-4 yields an expression for B in terms of A, γ, and $\Delta\gamma$. Expanding the denominator of this expression for B with respect to A and collecting terms by powers of A produces equation 7.

REFERENCES

Achenbach, J. D., 1973, Wave propagation in elastic solids: North-Holland Publishing Co.

Aki, K., and P. G. Richards, 1980, Quantitative seismology: Theory and methods, vol. 1: W. H. Freeman & Co.

Batzle, M. L., D. Han, and J. P. Castagna, 1995, Fluid effects on bright spot and AVO analysis: 65th Annual International Meeting, SEG, Expanded Abstracts, 1119–1121.

Brie, A., F. Pampuri, A. F. Marsala, and O. Meazza, 1995, Shear sonic interpretation in gas-bearing sands: 70th Annual Technical Conference, Society of Petroleum Engineers, Proceedings, 701–710.

Castagna, J. P., M. L. Batzle, and R. L. Eastwood, 1985, Relationships between compressional-wave and shear-wave velocities in clastic silicate rocks: Geophysics, **50**, 571–581.

Castagna, J. P., and S. W. Smith, 1994, Comparison of AVO indicators: A modeling study: Geophysics, **59**, 1849–1855.

Castagna, J. P., and H. W. Swan, 1997, Principles of AVO crossplotting: The Leading Edge, **16**, 337–342.

Castagna, J. P., H. W. Swan, and D. J. Foster, 1998, Framework for AVO gradient and intercept interpretation: Geophysics, **63**, 948–956.

Connolly, P., 1999, Elastic impedance: The Leading Edge, **18**, 438–452.

Domenico, S. N., 1977, Elastic properties of unconsolidated porous sand reservoirs: Geophysics, **42**, 1339–1368.

Fatti, J. L., G. C. Smith, P. J. Vail, P. J. Strauss, and P. R. Levitt, 1994, Detection of gas in sandstone reservoirs using AVO analysis: A 3-D seismic history using the Geostack technique: Geophysics, **59**, 1362–1376.

Foster, D. J., R. G. Keys, and D. P. Schmitt, 1997, Detecting subsurface hydrocarbons with elastic wavefields, *in* G. Chavent, G. Papanicolaou, P. Sacks, and W. Symes, eds., Inverse problems in wave propagation: Springer-Verlag, 195–218.

Foster, D. J., S. W. Smith, S. Dey-Sarkar, and H. W. Swan, 1993, A closer look at hydrocarbon indicators: 63rd Annual International Meeting, SEG, Expanded Abstracts, 731–734.

Goodway, W. N., T. Chen, and J. Downton, 1997, Improved AVO fluid detection and lithology discrimination using Lamé petrophysical parameters; "λρ," "μρ," and "λ/μ fluid stack," from P and S inversions: 67th Annual International Meeting, SEG, Expanded Abstracts, 183–186.

Gregory, A. R., 1976, Fluid saturation effects on dynamic elastic properties of sedimentary rocks: Geophysics, **41**, 895–921.

Keys, R. G., and D. J. Foster, eds., 1998, Comparison of seismic inversion methods on a single real data set: SEG.

Koefoed, O., 1955, On the effect of Poisson's ratios of rock strata on the reflection coefficients of plane waves: Geophysical Prospecting, **3**, 381–387.

Marion, D., A. Nur, H. Yin, and D. Han, 1992, Compressional velocity and porosity in sand-clay mixtures: Geophysics, **57**, 554–563.

Masters, A. R., S. Y. R. Gesbert, K. M. Wojcik, C. K. Chan, and L. P. Jong, 2009, Stalking uncertainty with Bayesian visualization: 71st Conference & Technical Exhibition, EAGE, Extended Abstracts, S026.

Mavko, G., T. Mukerji, and J. Dvorkin, 1998, The rock physics handbook: Cambridge University Press.

Muskat, M., and M. W. Meres, 1940, Reflection and transmission coefficients for plane waves in elastic media: Geophysics, **5**, 115–148.

Ostrander, W. J., 1984, Plane-wave reflection coefficients for gas sands at nonnormal angles of incidence: Geophysics, **49**, 1637–1648.

Rutherford, S. R., and R. H. Williams, 1989, Amplitude-versus-offset variations in gas sands: Geophysics, **54**, 680–688.

Shuey, R. T., 1985, A simplification of the Zoeppritz equations: Geophysics, **50**, 609–614.

Smith, G. C., and P. M. Gidlow, 1987, Weighted stacking for rock property estimation and gas detection: Geophysical Prospecting, **35**, 993–1014.

Smith, G. C., and R. A. Sutherland, 1996, The fluid factor as an AVO indicator: Geophysics, **61**, 1425–1428.

Verm, R., and F. Hilterman, 1995, Lithology color-coded seismic sections: The calibration of AVO crossplotting to rock properties: The Leading Edge, **14**, 847–853.